ACCSCIENCE PUBLISHING

Engineering Science in Additive Manufacturing

ORIGINAL RESEARCH ARTICLE

A machine learning approach for enhancing process screening and qualification in metal additive manufacturing

Ze Chen[1,2], Jingwen Gao[2], Chengcheng Wang[1], Zhuohong Zeng[1,2], Chenyang Zhu[2], and Wei Fan[1,3]*

[1]Singapore Centre for 3D Printing, Nanyang Technological University, Singapore

[2]School of Mechanical and Aerospace Engineering, Nanyang Technological University, Singapore

[3]State Key Laboratory of Solidification Processing, Northwestern Polytechnical University, Xi'an, Shaanxi, China

Abstract

The prevailing screening and qualification methodologies heavily depend on conventional manufacturing processes, which incur significant costs and prolonged lead times due to extensive physical testing. These challenges are also present in the growing field of additive manufacturing (AM), where numerous process parameters must be considered. However, the net-shape forming advantage of AM renders conventional screening and qualification methods inadequate. In the context of ongoing industrial digital transformation, a promising approach to enhancing process screening and qualification for metal AM is the adoption of a digital methodology tailored to the unique characteristics of this manufacturing technique. In this study, a convolutional neural network model is employed to extract features from images to predict material properties in laser-directed energy deposition (L-DED) processes. The model achieved a mean absolute percentage error of 2.3% and a root mean square error of 15.0 MPa for predicting ultimate tensile strength, with a prediction residual within ±1% for density. Unlike conventional approaches that rely on bulk or multilayer builds, this study uniquely demonstrates the feasibility of using early-stage single-track print features to predict final part properties with limited view and material involvement. This established model and workflow pave the way for highly efficient and low-cost property prediction in L-DED processes.

Keywords: Additive manufacturing; Directed energy deposition; Machine learning; Process screening; Qualification

***Corresponding author:**
Wei Fan
(fanw92@nwpu.edu.cn)

Citation: Chen Z, Gao J, Wang C, Zeng Z, Zhu C, Fan W. A machine learning approach for enhancing process screening and qualification in metal additive manufacturing. *Eng Sci Add Manuf*. 2025;1(3):025280018. doi: 10.36922/ESAM025280018

Received: July 9, 2025

1st revised: August 4, 2025

2nd revised: August 14, 2025

Accepted: August 14, 2025

Published online: August 30, 2025

Copyright: © 2025 Author(s). This is an Open-Access article distributed under the terms of the Creative Commons Attribution License, permitting distribution, and reproduction in any medium, provided the original work is properly cited.

Publisher's Note: AccScience Publishing remains neutral with regard to jurisdictional claims in published maps and institutional affiliations.

1. Introduction

Laser-directed energy deposition (L-DED) is a promising method for metal additive manufacturing (AM) and is widely used to fabricate net-shaped and near-net-shaped parts.[1,2] This technique enables the direct manufacture of highly complex parts from high-performance materials using computer-aided design data. Metal powder is fed either coaxially or through a set of radially symmetric nozzles into a molten pool created by laser energy during the L-DED process.[3] This material is deposited layer

by layer to fabricate a three-dimensional (3D) structure. The key to producing intricate structures using L-DED lies in identifying suitable process parameters.[4] Process parameters, such as power feed, scan speed, mass flow rate, and gas flow rate, play a crucial role in determining the final properties of additively manufactured parts.[5,6] Over the past decade, significant research efforts have focused on identifying optimal processing regimes for various materials to achieve defect-free manufacturing. These efforts have primarily relied on costly trial-and-error experiments and computationally expensive mechanistic simulations.[7]

The use of machine learning (ML) in materials engineering and smart manufacturing has been gaining popularity.[8,9] Researchers are increasingly adopting ML methods in metal AM to accelerate the development of process parameters and to reduce costs.[10] Utilizing ML enables the creation of process maps that provide a detailed view of the process windows, which aids in the efficient optimization of parameters.[11,12] This strategy helps researchers streamline the development of parameters, resulting in shorter development times and reduced costs from trial-and-error experiments. In addition, ML leverages extensive datasets to predict mechanical properties, expediting qualification and optimizing material selection and processing parameters.[13,14] This predictive capability integrates seamlessly with both in-process and post-process productive metrology, offering a comprehensive evaluation of manufactured components.[15,16]

The prevailing screening and qualification methodologies heavily rely on conventional manufacturing processes, such as casting, forging, and powder metallurgy. Consequently, these methodologies are associated with significant costs and prolonged lead times, primarily attributable to the extensive physical testing required. Moreover, it is imperative to acknowledge that these traditional approaches may not be well-suited for metal AM processes.[17] For L-DED, the flowchart of the prevailing traditional methods is shown in Figure 1A. The process begins with printing numerous single-bead samples based on experimental designs. These samples undergo several preparatory steps, including wire cutting, mounting, and polishing, to create metallurgical samples. These prepared samples are then examined under an optical microscope to capture the geometry index of the cross-sectional bead. Preliminary process window screening is carried out based on the bead geometry index, and the "good" parameters are selected for printing block samples. The final evaluation primarily focuses on the porosity and tensile properties of these block samples. Parameters that meet user-defined requirements are identified as the optimal process window. If the requirements are not met, the unsatisfactory parameters need to be revised. Depending on the complexity of the case, this may involve minor revisions for block printing or major redesigns for single-bead sample printing. The traditional methods can impose substantial costs and long lead times on commercial organizations due to insufficient qualification protocols.

Several prior studies in metal AM have applied convolutional neural networks (CNNs) to high-speed imaging data—particularly in powder bed fusion—to detect defects and predict properties. For example, Zhang *et al.*[18] achieved ~92.7 % classification accuracy recognizing quality levels from melt-pool, plume, and spatter images in stainlesssteel 316L single-track laser powder bed fusion. In addition, Herzog *et al.*[19] leveraged multi-axis infrared monitoring of completed builds, combined with ML, to detect defects in L-DED. Unfortunately, whether using *in situ* measurement data or full-build surface data, the acquisition workflow remains resource-intensive. AM inherently builds from lines (tracks) to volumes (parts); therefore, the quality of a single track could, to some extent, serve as fundamental feedback on final part quality. This is an intriguing yet underexplored proposition.

To address the constraints associated with the traditional method, this study introduces the ML-Qvision model, designed to achieve two primary functions: Function 1—rapid process window screening by scanning the surface profile of printed single-bead samples to predict the quality of the printed blocks using the CNN model—and Function 2—qualification of L-DED printed parts by scanning the surface profile of printed blocks to predict their porosity and tensile properties, as illustrated in Figure 1B. This study explores the use of ML techniques for screening process parameters and establishing surface-to-property relationships in L-DED fabricated Monel K-500 alloy. The novelty of this study lies in its use of surface profile images from single-bead tracks to predict final properties of L-DED builds. Traditional process screening and property qualification in AM typically require extensive multilayer printing and post-processing. In contrast, our approach enables early prediction of key quality metrics, potentially reducing the trial-and-error cycle in new material development, saving time, material, and cost.

2. Materials and methods

2.1. Directed energy deposition

The manufacturing process for all samples was conducted using the BeAM Magic 800 system (AddUp Group, France). Monel K-500 powder (Sandvik Osprey Ltd, United Kingdom), characterized by a size distribution ranging from 53 to 150 μm, was utilized for sample

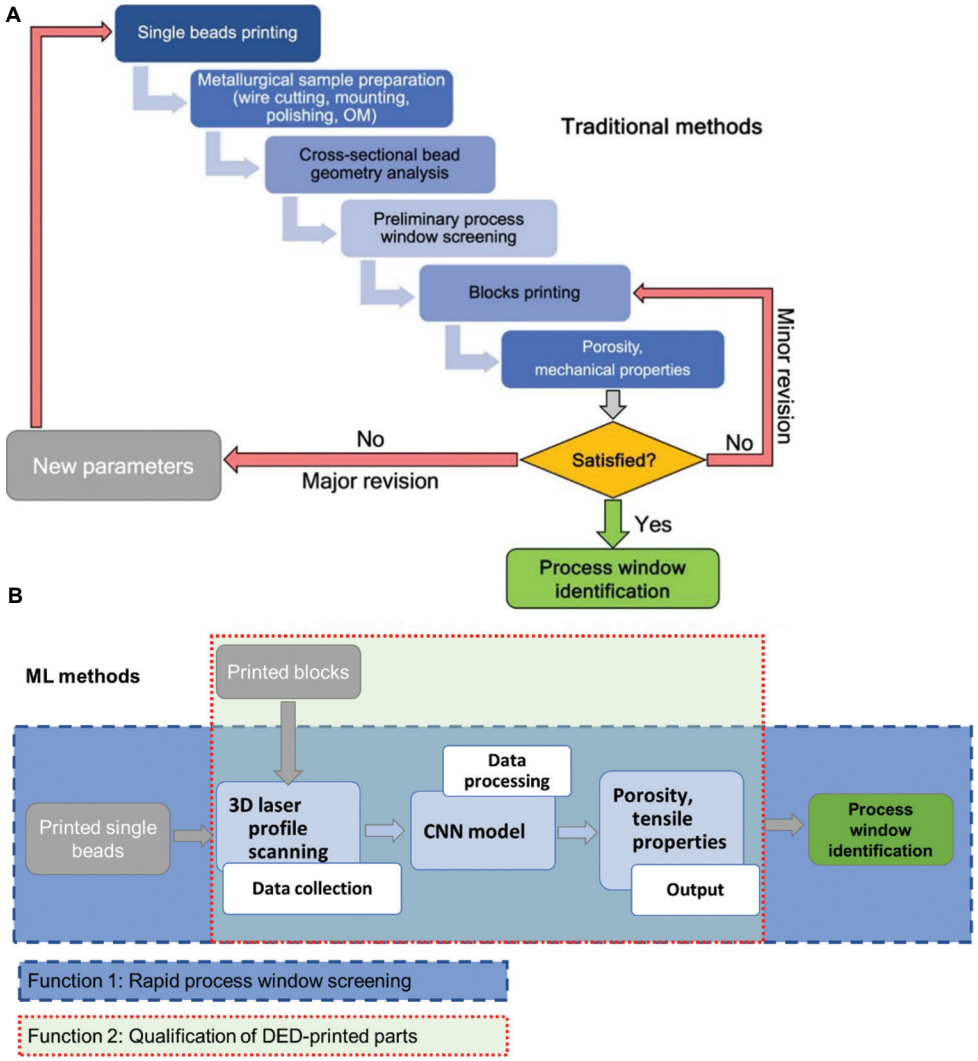

Figure 1. Schematic of proposed workflow and comparison with conventional methods
Abbreviations: 3D: Three-dimensional; CNN: Convolutional neural network; DED: Directed energy deposition; OM: Optical microscopy.

fabrication. The chemical composition of the powder is detailed in Table 1. Powder that is compatible with the L-DED process can achieve fully densified samples with optimal parameters.[4] Throughout the fabrication process, meticulous attention was devoted to capturing the surface morphology of the printed samples. In addition, the density of each block was carefully measured, with subsequent tensile testing exclusively administered to samples demonstrating the capability to yield valid results.

A full factorial design was employed to investigate the effect of three factors on the L-DED process, as detailed in Table 2. A total of $6 \times 7 \times 3 = 126$ combinations of process parameters were used for the L-DED process, encompassing both single-bead and block samples, to train the ML model. Notably, all single-bead samples were printed onto a single substrate and had a uniform length of 80 mm. The block samples generated possessed dimensions of 20 mm × 30 mm × 20 mm.

2.2. Materials characterization

The surface profiles of both printed blocks (Figure 2A) and single beads (Figure 2B) were captured by a laser profile sensor (LLT3010-25/BL, Micro-Epsilon, Germany), as shown in Figure 2C. The measured profiles were processed using the scanCONTROL 3D-View 3.7 software for illustration and image export. Before ML processing, all exported images were resized and set to a resolution of 650 × 650 pixels, which illustrates the surface roughness and continuity of the printed surface as a function of scan speed and laser power under the same feed rate. A complete dataset of the surface morphologies of both blocks and single beads is illustrated in Figure A1.

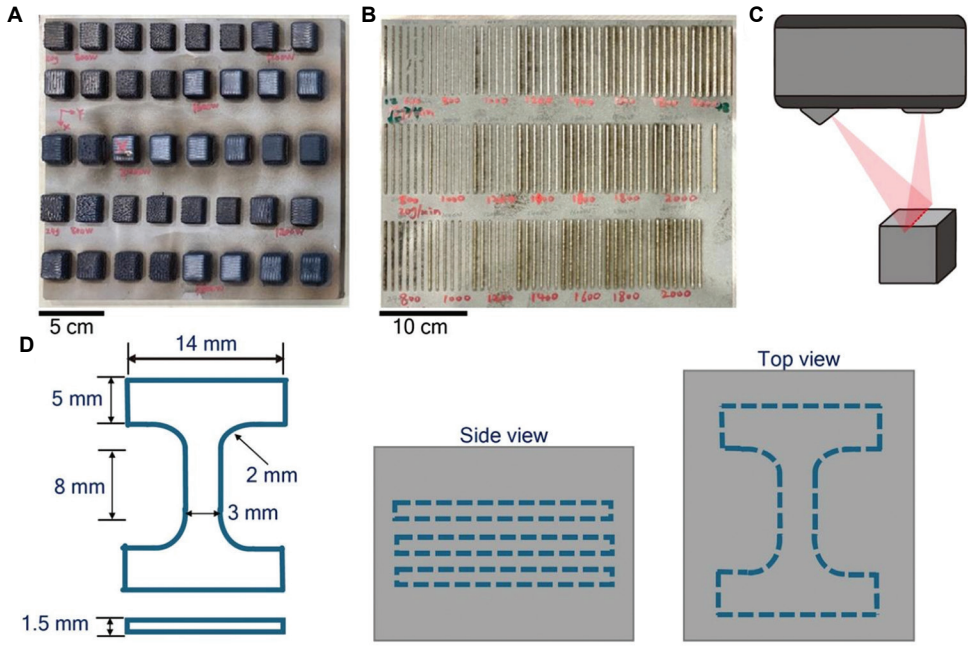

Figure 2. Experimental setups. (A) Printed blocks on the substrate. Scale bar: 5 cm. (B) Single beads on the substrate. Scale bar: 10 cm. (C) Schematic of a three-dimensional laser surface profile scanner. (D) Design of the tensile sample and the positions in the block sample.

Table 1. Chemical composition of the Monel K-500 powder

Element	Copper	Aluminum	Iron	Manganese	Titanium	Oxygen	Nickel
Percentage (wt%)	30	2.35	1.2	1.1	0.82	0.01	Bal.

Table 2. Parameters used for laser-directed energy deposition

Parameters	Value
Laser power (W)	800, 1,000, 1,200, 1,400, 1,600, 1,800, 2,000
Scanning speed (mm/min)	1,000, 1,400, 1,800, 2,200, 2,600, 3,000
Powder feed rate (g/min)	16, 20, 24
Secondary gas flow rate (L/min)	10
Central gas flow rate (L/min)	6
Laser spot size (mm)	2.25
Z step (mm)	0.3, 0.45
XY step (mm)	1.5
Powder carrier gas level	60%

Density measurement was only conducted on block samples. Block samples were wire cut from the substrate, and densities were determined via Archimedes' method using a densitometer (XS204; Mettler Toledo, United States). After acquiring the densities of the blocks, the samples were shaped into dog-bone specimens using electrical discharge machining for tensile testing. The design of the tensile coupons is shown in Figure 2D. Three specimens were cut from the printed block samples from the middle part. Several samples were excluded due to printing defects, such as pores and lack of fusion, as illustrated in Figure A2. Only 61 samples qualified for tensile testing to acquire the ultimate tensile strength (UTS) and elongation at failure. The tensile tests were conducted on a uniaxial tester (AGX 50 KN, Shimadzu, Japan) with a non-contact digital video extensometer, with a strain rate of 0.5 mm/min at room temperature. Testing was conducted on each block sample using three identical tensile coupons.

2.3. ML framework

A CNN is a robust neural network architecture for image-related tasks, including classification and regression.[20] It can automatically detect the critical features from raw images without manual supervision. As surface morphology images are the inputs for the predictive model training in this research work, CNN handles the image dataset and establishes the surface-to-property relationships.

2.3.1. Model implementation

The ML-Qvision framework was implemented in the Python Tensorflow library (version 2.1.0) using the Keras

functional application programming interface.[21] This model, as schematically illustrated in Figure 3, has three pairs of convolutional and pooling layers followed by three fully connected layers. The number of filters for the three convolutional layers was set as 16, 32, and 64, respectively, to capture different pattern combinations from the images. The size of each filter was 3 × 3, followed by a "same" padding. The output generated by each convolutional layer was fed into a max pooling layer to obtain a down-sampled feature map. The max pooling layers have a pool size of 2 × 2, halving the dimensions in horizontal and vertical directions. The feature map generated by the last max pooling layer was flattened into a vector and then fed to the first fully connected layer. The number of nodes in the three fully connected layers was 16, 4, and *N*, where *N* depends on the required number of outputs. For the case of only one output, a total of 89,721 trainable parameters were leveraged in the model. Batch normalization and dropout with a rate of 0.4 were applied only after the first fully connected layer to prevent overfitting. The output layer used the linear activation function for the regression task. The model was trained with 1000 epochs and a batch size of eight. The train-test split ratio was 80/20, as a general practice.

The input images are represented with dimensions n × n × m, where *n* is the width and height of the surface morphology image, and *m* is the number of channels (for a color image, *m* = 3 for red, green, and blue channels, whereas *m* = 1 for grayscale images). All input images were normalized from the original range of 0–255 to a standardized range of 0–1 before being input into the CNN. This normalization reduces computational complexity and accelerates model convergence.

2.3.2. Objective functions

Error metrics designed for numeric values were used to evaluate predictions made by regression models. These metrics provide an indicative score that summarizes the predictive performance of the trained model, allowing users to compare accuracy across different model settings and datasets. The two most commonly used error metrics for regression predictions are mean absolute percentage error (MAPE) and root mean square error (RMSE).[22] MAPE is the mean of all absolute percentage errors between the predicted and actual values, whereas RMSE is the square root of the mean squared error between the predicted and actual values. MAPE expresses the error as a percentage, facilitating easier model comparisons, whereas RMSE is on the same scale as the target variable. However, MAPE is more sensitive to outliers, as it can produce significant percentage errors when the target value is very small. Consequently, both MAPE and RMSE were monitored to predict density and tensile properties.

2.3.3. k-fold cross-validation

Model performance validation is essential for ensuring the accuracy of any predictions of an ML model. Typically, the unseen data (test set) is separated from the overall dataset using a user-defined ratio; for instance, an 80/20 ratio is set for this model training and testing. However, this splitting can introduce bias if the data distribution in the test set significantly differs from the training set, a problem that is more pronounced with limited data. Cross-validation is a technique used to evaluate ML models on limited datasets.[23,24] It provides a more robust estimate of the trained model's generalization error.

In *k*-fold cross-validation, the dataset was first shuffled to ensure that the order of the inputs and outputs was utterly random. This step helps to ensure that the data are less biased. Then, the dataset was split into *k* non-overlapping subsets of equal size. Each *k*-subset was treated as a test set, whereas all other subsets were collectively used as a training set. The overall model performance was calculated as the mean of the *k* hold-out test performances. *k*=5 was chosen for this analysis on the small dataset.[23]

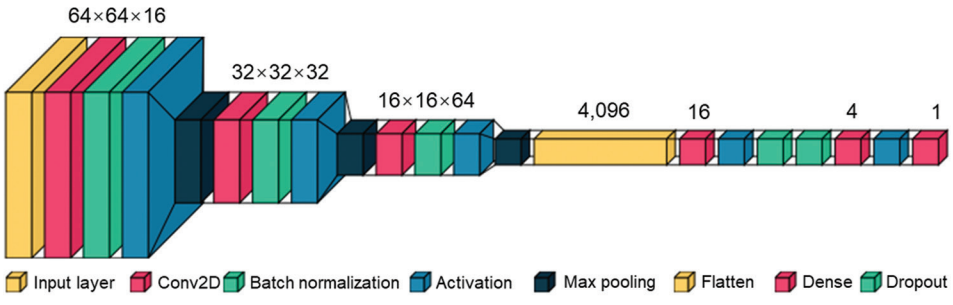

Figure 3. Convolutional neural network architecture used for feature extraction from surface profile images
Abbreviation: conv2D: Two-dimensional convoluted layer.

3. Results

3.1. Dataset collection and data processing

Input data for the ML model is separated into two parts: (i) The input surface profile images, and (ii) the targeted properties for the regression work, including density and tensile properties (UTS and elongation at failure). For every processing parameter combination of scan speed, power, and feed rate, two profiles from the printed block surface and the single-bead surface were collected. A top view of this 3D profile, color-coded by the height of the sample surface, was used as raw images for the input. Each raw color image was first resized to the pre-determined input size of 64 × 64. The RGB images were then normalized to a range of (0, 1) by dividing the raw values by 255. In this sense, a total of 126 images of block top surface and 126 images of single-bead surface were generated from the measured surface profile as the input for the model training process. Figure 4A shows the input images matrix printed at a fixed feed rate of 16 g/min, while varying the other two processing parameters. The inputs for the other two feed rate conditions are shown in Figure A1. The block surface morphology changed significantly with varying power and scan speed, as shown in Figure 4A. Lower scan speeds combined with higher power resulted in rougher and more textured surfaces, whereas higher scan speeds and lower power produced smoother surfaces with fewer pronounced features. When the same parameters were applied to print single-bead samples, higher power enhanced the intensity of the red lines, indicating higher regions, while lower power resulted in less pronounced features. In addition, processing parameters that produce a rough block surface also resulted in a thinner, less smooth surface. This correlation in surface features suggests that the bulk sample surface can be inferred from the single-bead surface, enabling predictions for the larger sample based on observations of the bead surface.

The metrics for the properties on the output side of the Qvision model are density and tensile properties. The densities of all 126 block samples are plotted in Figure 4B. For all types of feed rate, the defect samples—typically with lower densities—were consistently observed at lower power levels and higher scan speeds. Notably, the printed material, Monel 400 nickel-based super alloy, has a nominal density of around 8.5 g/cm^3. When laser power is above 1200 W, the printed blocks are close to the nominal density and are considered nearly dense. Tensile coupons were cut from these printed blocks. However, only 61 of them were free of defects—such as large poles and a lack of interior fusion defects—at the designed positions. The existence and the distribution of defects could significantly detriment the tensile properties of the blocks. Blocks that could not produce tensile coupons with minimal macroscopic defects were excluded as potential outliers. Measured tensile properties for the 61 qualified parameter combinations are plotted in Figure 4C and categorized by powder feed rate. The 16 g/min and 24 g/min feed rates showed more variability in both metrics of tensile properties, with noticeable clusters indicating optimal ranges. In contrast, the 20 g/min feed rate exhibited a more consistent performance, with less variability in both UTS and elongation. It achieved higher UTS values while maintaining moderate elongation.

3.2. Process window screening

Process window screening is a critical method for evaluating and optimizing printing process parameters within a defined range to achieve the desired printing outcomes. This approach involves systematically varying and analyzing factors such as laser power, scan speed, and powder feed rate to identify the optimal combination that yields the best print quality and mechanical properties. By adjusting these parameters, manufacturers can fine-tune the printing process to produce parts that meet stringent specifications and performance standards.

For the L-DED fabricated Monel K-500 alloy, density and UTS values predicted from surface profiles of printed single-bead samples were used as screening references. A scatter plot relating these two properties is shown in Figure 5A. According to the specific application requirements, users can define acceptable thresholds for both UTS and density to differentiate satisfactory printed samples from unsatisfactory ones. In this study, the threshold values selected were a UTS of at least 500 MPa and a density greater than 8.4 g/cm^3. These criteria were used to establish a qualified region within the scatter plot, which was shaded green for visual clarity in Figure 5A. Within this qualified region, a total of 21 samples met the defined criteria, although three of these were excluded from further tensile testing. The samples that did not meet the criteria and fell outside the green shaded region were disqualified. It was observed as the inset of Figure 5A that the qualified samples within the green region exhibited relatively smoother surfaces and fewer discontinuities in the single-bead surface profile. This was consistent with the expectations, as stronger (higher UTS) and denser (higher density) samples typically correlate with better overall sample quality and fewer defects in printed materials. A comprehensive visual representation is shown in Figure 5B, in which red circles represent the process parameters that produced a disqualified sample due to either poor tensile properties or low density, and green surfaces enclose all the qualified processing parameter combinations, which indicate the optimized process window.

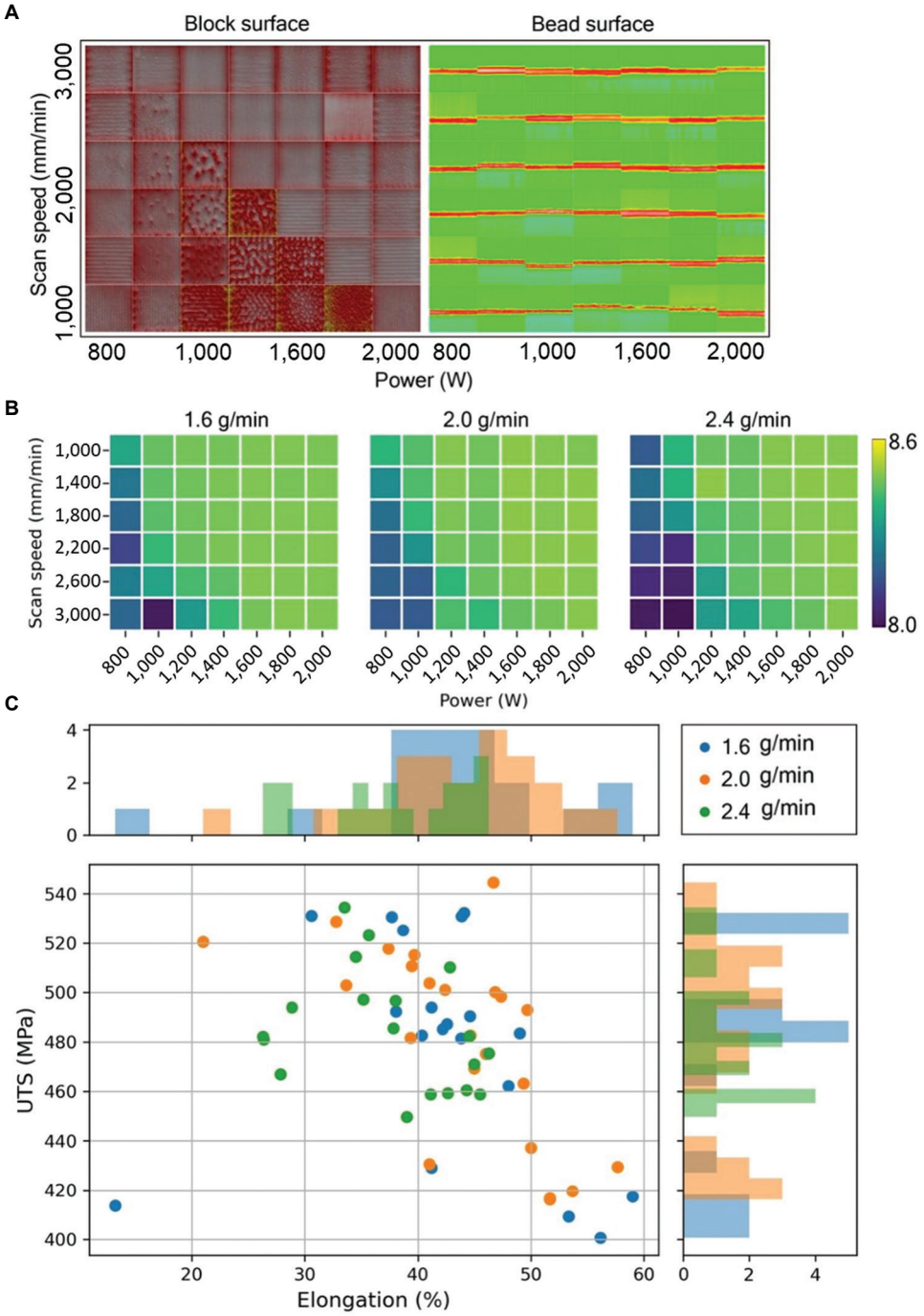

Figure 4. Measured data for Qvision model training. (A) Surface profile for both block and single-bead samples for powder feed rate of 16 g/min. (B) Measured density for all 126 block samples as a function of three variables. (C) Tensile properties (ultimate tensile strength and elongation at failure) for 61 qualified block samples that could produce a valid tensile coupon for uniaxial tensile testing.

3.3. Input image size tuning

CNNs can process input of arbitrary size by applying a combination of downsampling and pooling. However, it has been found that CNN models are not agnostic to the input size;[25] they exhibit significant differences in performance based on the input size. Presenting the same image at different scales can result in varying outcomes.[26] There is no straightforward relationship between input

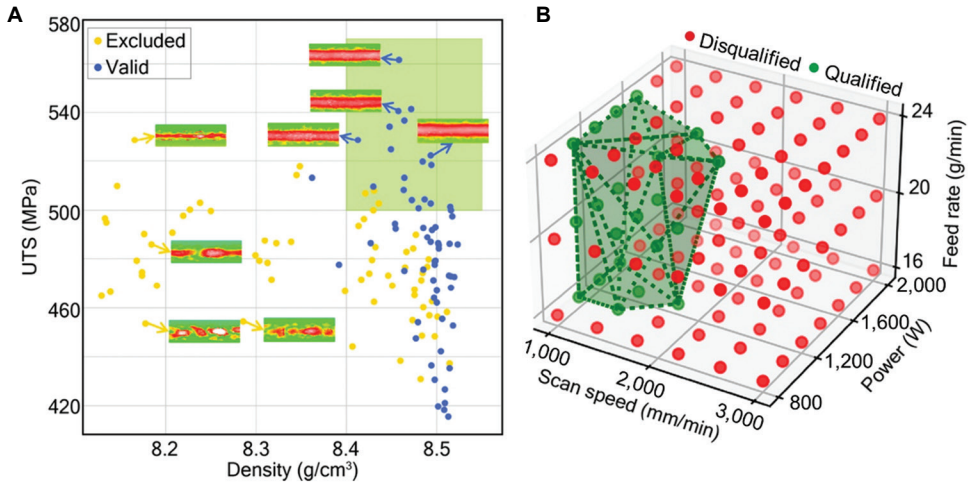

Figure 5. Print parameter screening. (A) Scatter plot of ultimate tensile strength versus density for printed single-bead samples and its role in identifying the qualification region. (B) Three-dimensional plot unveils process window with parameters and qualification status.

size and model performance; instead, each network has an optimal input size at which it performs best. Therefore, three different input image sizes (32 × 32, 64 × 64, 128 × 128) were investigated before training the final model to determine an optimal value that can yield more accurate prediction results.

Figure 6 reveals that the performance of the CNN model varies significantly with different input image sizes. For both density and UTS predictions, the error metrics (MAPE and RMSE) showed a similar trend. The optimal performance for both properties was observed at an image size of 64 × 64, where the MAPE and RMSE values were the lowest. This indicated that the model could achieve the highest accuracy and lowest prediction error at this image size. In contrast, smaller (32 × 32) or larger (128 × 128) image input would increase error metrics, suggesting a decrease in model performance. Interestingly, although higher resolution (128 × 128) retained more spatial information, its use led to degraded performance compared to the 64 × 64 size. The reduced accuracy with a smaller input size is expected, as the limited resolution provides insufficient spatial information for reliable predictions. In contrast, although a larger input size of 128 × 128 retained finer details and higher resolution, the model performance did not improve as anticipated. The enlarged input size introduced a greater number of redundant features, increasing the risk of overfitting and complicating the feature–target relationships beyond the capacity of the current network architecture. In small-data settings, richer input can exacerbate overfitting due to the curse of dimensionality, where the required number of training samples grows exponentially with input feature dimensionality.[27] Furthermore, higher resolution increases the number of learned parameters, potentially exceeding the model capacity for this dataset and reducing generalization ability. These observations confirmed that each model exhibits an optimal input size, and in this case, the size of 64 × 64 yielded the best results for predicting both density and UTS.

3.4. Performance evaluation

After validating the proposed CNN model using the five-fold cross-validation, a new model was trained with a single output on a newly split training set for predicting sample density and tensile properties. Notably, for one process parameter, printing was conducted for both the block and a single bead. The output metrics, the properties of the printed sample, were measured and selected from block samples only. Two models were trained on different input surface profiles from single beads and blocks, respectively. All test cases were close to the blue regression line, on which the predicted and actual densities were the same, as shown in Figure 7A, except for an obvious outlier for single beads. The block samples exhibited higher prediction accuracy compared to single bead samples, as indicated by the higher R^2 value. The residual analysis shown in Figure 7B also indicates that the predicted outcome varies within a ±1% range of the ground truth values. In addition, the calculated residuals did not exhibit a visible pattern, i.e., the error is independent of predicted density value, indicating that the model is a good fit for the density prediction. A higher indexing accuracy was achieved for samples with a density over 8.4 g/cm³, which is close to the completely dense state. The model performed better as the number of dense samples for the training input was greater than that of defective ones with lower density, as shown in Figure 4B. A more evenly distributed dataset could be used for model training to achieve a more reliable prediction.

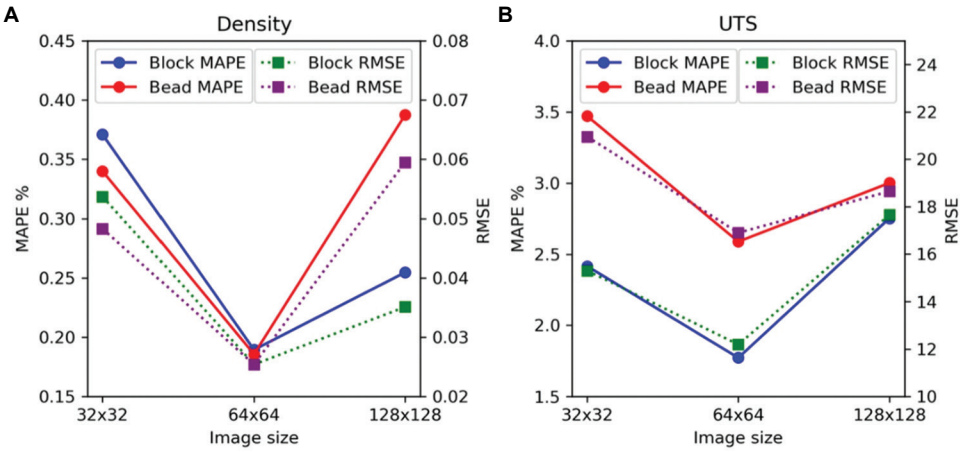

Figure 6. Model performance to compare results for block and bead samples across different image sizes. (A) Density. (B) UTS. Abbreviations: MAPE: Mean absolute percentage error; RMSE: Root mean square error; UTS: Ultimate tensile strength.

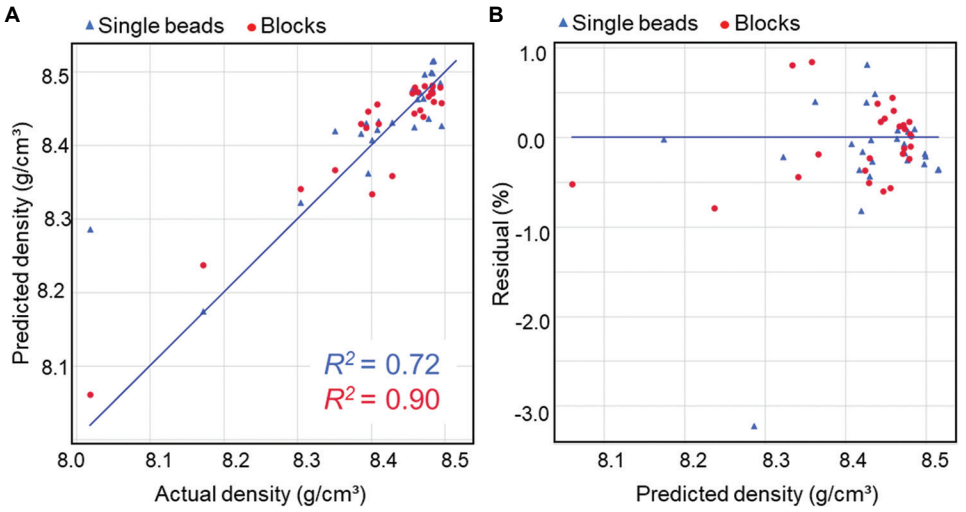

Figure 7. Surface to density prediction result. (A) Plot of predicted versus measured densities for single-bead and block samples, and (B) the corresponding residual plot.

Figure 8A shows the predicted versus measured UTS for single-bead and bulk samples based on the testing surface profiles (the input images). Both the R^2 values of single-bead and block samples are lower than 0.5. The predicted values are more scattered from the ground truth line, and higher residuals (±5%) were found for the model predicting UTS compared to the density prediction (±1%), as illustrated in Figure 8B. This reduced accuracy can be partly attributed to the limited dataset size, as only 61 samples were available for training and testing the UTS prediction model. The model had fewer examples from the full UTS range, which likely contributed to the increased complexity in learning the relationship. Furthermore, UTS prediction is inherently more challenging than density prediction, as tensile strength depends on multiple factors beyond porosity, including grain structure, phase composition, and defect morphology, many of which are not fully captured in surface profile images. In contrast, density is more directly related to surface-visible features, such as lack-of-fusion defects or irregular melt tracks, making it easier for the model to establish a consistent mapping. Nevertheless, the performance of UTS prediction from single-bead samples was comparable with that from block surfaces. The model's ability to exploit the additional geometric and textural information present in block surface profiles was constrained by the limited data size. As a result, both input types provided a similar level of predictive capability for UTS within the current data conditions. A larger and more diverse dataset could potentially reveal clearer performance differences between the two input types.

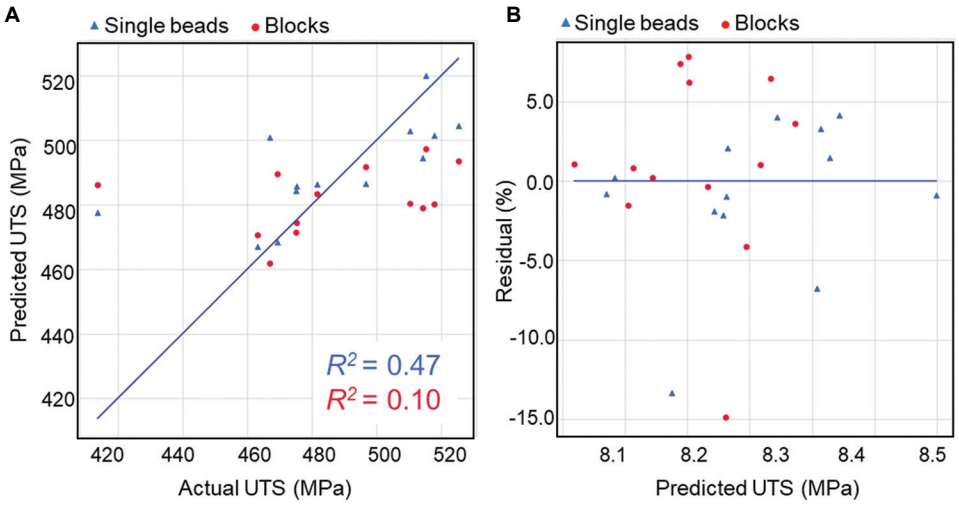

Figure 8. Surface to UTS prediction result. (A) Plot of predicted UTS versus measured UTS for single-bead and block samples, and (B) the corresponding residual plot.
Abbreviation: UTS: Ultimate tensile strength.

Apart from UTS, elongation at failure was also predicted. Numerous studies have reported a systematic strength-ductility trade-off across metallic systems, where UTS tends to increase as elongation decreases, reflecting shared but competing structural influences. This relationship motivated the development of a multi-output regression model, featuring a shared convolutional backbone and separate fully connected output heads for UTS and elongation. The expectation was that shared layers could capture common predictive features from surface profiles, enabling knowledge transfer[28] and improving both outputs. However, as shown in Table 3, the multi-output model produced higher MAPE and RMSE values than the corresponding single-output models. The differences in error between the single-output model and multi-output model for UTS and elongation are 1.3% and 2.3%, respectively. This result indicates that while UTS and elongation share some dependencies, they are not perfectly correlated in terms of predictive features extracted from surface images. In the context of the current small dataset, this partial overlap may have limited the benefit of shared feature learning, leading instead to negative knowledge transfer. Another contributing factor could be the curse of dimensionality.[29] Increasing the dimensionality of the output space without a corresponding increase in sample size raises the computational complexity of the learning problem and the risk of overfitting, ultimately reducing prediction accuracy.

Table 3. Performance comparison for single and multi-output convolutional neural network models

Model type	MAPE %		RMSE	
	UTS	Elongation	UTS	Elongation
Single-output	2.3	6.9	15.0	3.1
Multi-output	3.6	9.2	21.6	4.5

Abbreviations: MAPE: Mean absolute percentage error; RMSE: Root mean square error; UTS: Ultimate tensile strength.

4. Discussion

The proposed ML-Qvision model uses image input that offers distinct advantages over traditional process parameters. Images inherently contain a wealth of information with intricate spatial relationships, which provides a more comprehensive representation of the subject matter compared to numerical or categorical data alone.[30] In this study, the smoothness of the surface profile, discontinuous sites (originating from the surface roughness), and relative intensity variation (resulting from the height difference of the surface) on the corresponding input images provided valuable insights to the model. The top surface is an essential indicator of the part's overall quality, i.e., the final properties of built samples.[31] It also reflects the quality of the laser-material interaction during the building process and can be used to reveal potential issues such as overheating, insufficient melting, or improper layer bonding. Qualitatively, insufficient energy input during the printing process can induce lack of fusion defects and leave behind unmelted powders, resulting in a porous surface post-melting.[32] Conversely, excessive energy input may cause spherical pores and bubbles due to the Marangoni flow in the melt pool.[33,34] An uneven or wavy surface may correlate with internal defects, whereas an ideal surface would exhibit minimal surface roughness,

indicating a defect-free internal structure. Thus, a well-processed surface often correlates with a sound internal microstructure, while surface imperfections can indicate underlying issues within the material.

The trained ML-Qvision eliminates the need for manual feature extraction and analysis, often required when using process parameters, thereby streamlining the data preparation phase and reducing potential human error. In this work, the accuracy of density prediction significantly surpasses that of tensile properties. The key distinction lies in the quantity of valid input data available for model training. Out of all 126 fabricated samples, only 61 samples successfully generated images paired with corresponding measured data for predicting tensile properties from the surface profile. CNN models generally necessitate substantial datasets to accurately capture intricate patterns and relationships within the data. In scenarios where the available data is limited, the model may struggle to effectively learn complex features, resulting in suboptimal performance.[35] Increasing the number of inputs could improve the performance of the model. However, L-DED samples produced under certain processing parameters are prone to defects, which hinder the production of valid tensile coupons. Despite defective samples being inevitable within these process parameters—due to issues such as lack of fusion or extensive porosity commonly found in unsuitable metal AM parameters.[36,37]—including more input data for the tensile property prediction model would enhance its accuracy and versatility. In the meantime, the defects mentioned above could be predicted by the proposed model, enriching the information that is deduced from the simple surface profile measurement. Obtaining this information for printed samples typically requires X-ray tomography scans or destructive screening by microscopes.[38,39] In the context of CNN models with multiple outputs, leveraging the correlation between outputs can be highly informative and productive.[27] Future research could be directed toward developing an image data-driven model capable of simultaneously predicting defects and tensile properties, in which the eliminated data due to defects can be utilized.

The current workflow aimed to correlate surface profile data with the properties of the samples. The trained model achieved comparable prediction performance when a full image of a block surface and a single line from a single-bead sample were used. This indicates that properties can be effectively predicted based on the surface profile image of a single bead during the L-DED process. Consequently, property inspection does not require a fully built sample for testing, which typically involves tedious and destructive sample preparation procedures. Instead, the quality inspection of required properties, such as density and tensile strength, can be predicted by capturing the surface profile of a single track. This approach streamlines the inspection process, reducing the time and material costs associated with traditional testing methods. In addition, the L-DED process is conducted in a line-by-line and layer-by-layer manner. Capturing the surface profile during the printing process has been successful using various vision systems, such as laser and structured light-based techniques.[40,41] By implementing the trained model into monitoring techniques for the printed surface profile, it is possible to perform *in situ* monitoring of the surface and accurately deduce the related properties of the sample. This integration allows for real-time quality assessment during the printing process, enhancing efficiency and reducing the need for post-production testing.

5. Conclusion

An ML approach enables rapid property prediction and process screening for additively manufactured alloys. This study introduced ML-Qvision, a CNN-based model designed to predict the density and tensile properties of laser-DED Monel K-500 alloy from surface morphology profiles. The predicted densities showed a strong correlation with the tested data. In addition to predicting densities and tensile properties from the whole block surface morphology, the model achieved comparable prediction performance by training on single-bead surfaces printed using the same processing parameters. The study provides evidence that printed surfaces with clear melt lines and smooth features correlate with higher density (lower porosity) and higher UTS, consistent with experimental findings. This suggests that the ML model accurately identified important predictive features. The proposed approach paves the way for using ML-Qvision for quick and robust process parameter screening from a single-bead print surface and quality assessment from bulk surfaces. In addition, this approach demonstrates versatility, making it applicable to other metal AM techniques and various material systems.

Acknowledgments

None.

Funding

This work was supported by the Fundamental Research Funds for the Central Universities (Grant No. D5000250077).

Conflict of interest

Wei Fan is an Editorial Board Member of this journal, but was not in any way involved in the editorial and peer-review

process conducted for this paper, directly or indirectly. Separately, other authors declared that they have no known competing financial interests or personal relationships that could have influenced the work reported in this paper.

Author contributions

Conceptualization: Ze Chen, Wei Fan
Formal analysis: Wei Fan
Investigation: Chengcheng Wang, Zhuohong Zeng, Chenyang Zhu
Methodology: Jingwen Gao
Writing–original draft: Ze Chen
Writing–review & editing: Wei Fan

Ethics approval and consent to participate

Not applicable.

Consent for publication

Not applicable.

Availability of data

The data presented in this study are available upon request from the corresponding author.

References

1. Svetlizky D Das M Zheng B *et al.* Directed energy deposition (DED) additive manufacturing: Physical characteristics defects challenges and applications. *Mater Today*. 2021;49:271-295.

   doi: 10.1016/j.mattod.2021.03.020.

2. Ahn DG. Directed energy deposition (DED) process: State of the art. *Int J Precis Eng Manuf Green Tech*. 2021;8:703-742.

   doi: 10.1007/s40684-020-00302-7

3. Guner A, Bidare P, Jiménez A, Dimov S, Essa K. Nozzle designs in powder-based direct laser deposition: A review. *Int J Precis Eng Manuf*. 2022;23:1077-1094.

   doi: 10.1007/s12541-022-00688-1

4. Chen Z, Wang C, Tang C, *et al.* Microstructure and mechanical properties of a Monel K-500 alloy fabricated by directed energy deposition. *Mater Sci Eng A*. 2022;857:144113.

   doi: 10.1016/j.msea.2022.144113

5. Ostolaza M, Arrizubieta JI, Queguineur A, Valtonen K, Lamikiz A, Flores II. Influence of process parameters on the particle-matrix interaction of WC-Co metal matrix composites produced by laser-directed energy deposition. *Mater Des*. 2022;223:111172.

   doi: 10.1016/j.matdes.2022.111172

6. Eisenbarth D, Stoll P, Klahn C, Heinis TB, Meboldt M, Wegener K. Unique coding for authentication and anti-counterfeiting by controlled and random process variation in L-PBF and L-DED. *Addit Manuf*. 2020;35:101298.

   doi: 10.1016/j.addma.2020.101298

7. Stavropoulos P, Foteinopoulos P. Modelling of additive manufacturing processes: A review and classification. *Manuf Rev*. 2018;5:2.

   doi: 10.1051/mfreview/2017014

8. Stavropoulos P, Sabatakakis K, Papacharalampopoulos A, Mourtzis D. Infrared (IR) quality assessment of robotized resistance spot welding based on machine learning. *Int J Adv Manuf Technol*. 2022;119:1785-1806.

   doi: 10.1007/s00170-021-08320-8

9. Wang J, Zhang X, Lu Y. Machine learning in image-based metal additive manufacturing process monitoring and control: A review. *Eng Sci Addit Manuf*. 2025;1(1):8548.

   doi: 10.36922/esam.8548

10. Johnson NS, Vulimiri PS, To AC, *et al.* Invited review: Machine learning for materials developments in metals additive manufacturing. *Addit Manuf*. 2020;36:101641.

    doi: 10.1016/j.addma.2020.101641

11. Zhang M, Sun CN, Zhang X, *et al.* High cycle fatigue life prediction of laser additive manufactured stainless steel: A machine learning approach. *Int J Fatigue*. 2019;128:105194.

    doi: 10.1016/j.ijfatigue.2019.105194

12. Tapia G, Khairallah S, Matthews M, King WE, Elwany A. Gaussian process-based surrogate modeling framework for process planning in laser powder-bed fusion additive manufacturing of 316L stainless steel. *Int J Adv Manuf Technol*. 2018;94:35913603.

    doi: 10.1007/s00170-017-1045-z

13. Zhu K, Fuh JYH, Lin X. Metal-based additive manufacturing condition monitoring: A review on machine learning based approaches. *IEEE/ASME Trans Mechatron*. 2021;27:2495-2510.

    doi: 10.1109/tmech.2021.3110818

14. Qi X, Chen G, Li Y, Cheng X, Li C. Applying neural-network-based machine learning to additive manufacturing: Current applications, challenges and future perspectives. *Engineering*. 2019;5:721-729.

    doi: 10.1016/j.eng.2019.04.012

15. Zhang Y, Yan W. Applications of machine learning in metal powder-bed fusion in-process monitoring and control: Status and challenges. *J Intell Manuf*. 2023;34:2557-2580.

    doi: 10.1007/s10845-022-01972-7

16. Zhang X, Saniie J, Heifetz A. Detection of defects in additively manufactured stainless steel 316L with compact infrared camera and machine learning algorithms. *JOM*. 2020;72:4244-4253.

    doi: 10.1007/s11837-020-04428-6

17. Achillas C, Tzetzis D, Raimondo MO. Alternative production strategies based on the comparison of additive and traditional manufacturing technologies. *Int J Prod Res*. 2017;55:3497-3509.

doi: 10.1080/00207543.2017.1282645

18. Zhang Y, Hong GS, Dongsen Y, *et al.* Extraction and evaluation of melt pool plume and spatter information for powder-bed fusion AM process monitoring. *Mater Des*. 2018;156:458-469.

doi: 10.1016/j.matdes.2018.07.002

19. Herzog T, Brandt M, Trinchi A, *et al.* Process monitoring and machine learning for defect detection in laser-based metal additive manufacturing. *J Intell Manuf*. 2024;35:1407-1437.

doi: 10.1007/s10845-023-02119-y

20. Seddiki K, Saudemont P, Precioso F, *et al.* Cumulative learning enables convolutional neural network representations for small mass spectrometry data classification. *Nat Commun*. 2020;11:1-11.

doi: 10.1038/s41467-020-19354-z

21. Abadi M, Barham P, Chen J, *et al.* TensorFlow: A System for Large-Scale Machine Learning. In: *Proceedings of the 12th USENIX Conference on Operating Systems Design and Implementation*. USENIX Association; 2016. p. 265-283.

22. Lv R, Yuan Z, Lei B. A high-fidelity digital twin predictive modeling of air-source heat pump using FCPM-SBLS algorithm. *J Build Eng*. 2024;87:109082.

doi: 10.1016/j.jobe.2024.109082

23. Xiong Z, Cui Y, Liu Z, Zhao Y, Hu M, Hu J. Evaluating explorative prediction power of machine learning algorithms for materials discovery using k-fold forward cross-validation. *Comput Mater Sci*. 2020;171:109203.

doi: 10.1016/j.commatsci.2019.109203

24. Zhang Y, Ling C. A strategy to apply machine learning to small datasets in materials science. *NPJ Comput Mater*. 2018;4:25.

doi: 10.1038/s41524-018-0081-z

25. Rukundo O. Effects of image size on deep learning. *Electronics*. 2023;12:985.

doi: 10.3390/electronics12040985

26. Richter ML, Byttner W, Krumnack U, Wiedenroth A, Schallner L, Shenk J. (Input) size matters for CNN classifiers. In: Farkaš I, Masulli P, Otte S, Wermter S, editors. *Artificial Neural Networks and Machine Learning - ICANN 2021*. Berlin: Springer International Publishing; 2021. p. 133-144.

doi: 10.1007/978-3-030-86340-1_11

27. Thambawita V, Strumke I, Hicks SA, Halvorsen P, Parasa S, Riegler MA. Impact of image resolution on deep learning performance in endoscopy image classification: An experimental study using a large dataset of endoscopic images. *Diagnostics (Basel)*. 2021;11:2183.

doi: 10.3390/diagnostics11122183

28. Yu H, Yang K, Zhang L, *et al.* Multi-output ensemble deep learning: A framework for simultaneous prediction of multiple electrode material properties. *Chem Eng J*. 2023;475:146280.

doi: 10.1016/j.cej.2023.14628

29. Bessa MA, Bostanabad R, Liu Z, *et al.* A framework for data-driven analysis of materials under uncertainty: Countering the curse of dimensionality. *Comput Methods Appl Mech Eng*. 2017;320:633-667.

doi: 10.1016/j.cma.2017.03.037

30. Ling J, Hutchinson M, Antono E, DeCost B, Holm EA, Meredig B. Building data-driven models with microstructural images: Generalization and interpretability. *Mater Discov*. 2017;10:19-28.

doi: 10.1016/j.md.2018.03.002

31. Gui Y, Aoyagi K, Bian H, Chiba A. Detection classification and prediction of internal defects from surface morphology data of metal parts fabricated by powder bed fusion type additive manufacturing using an electron beam. *Addit Manuf*. 2022;54:102736.

doi: 10.1016/j.addma.2022.102736

32. Thompson SM, Bian L, Shamsaei N, Yadollahi A. An overview of direct laser deposition for additive manufacturing; Part I: Transport phenomena modeling and diagnostics. *Addit Manuf*. 2015;8:36-62.

doi: 10.1016/j.addma.2015.07.001

33. Zhang K, Chen Y, Marussi S, *et al.* Pore evolution mechanisms during directed energy deposition additive manufacturing. *Nat Commun*. 2024;15:1715.

doi: 10.1038/s41467-024-45913-9

34. Kuriya T, Koike R, Mori T, Kakinuma Y. Relationship between solidification time and porosity with directed energy deposition of inconel 718. *J Adv Mech Des Syst Manuf*. 2018;12:Jamdsm0104.

doi: 10.1299/jamdsm.2018jamdsm0104

35. Thanapol P, Lavangnananda K, Bouvry P, Pinel F, Leprévost F. Reducing Overfitting and Improving Generalization in Training Convolutional Neural Network (CNN) Under Limited Sample Sizes in Image Recognition. In: *2020 - 5th International Conference on Information Technology (InCIT)*; 2020. p. 300-305.

doi: 10.1109/incit50588.2020.9310787

36. Brennan MC, Keist JS, Palmer TA. Defects in metal additive manufacturing processes. *J Mater Eng Perform*. 2021;30:4808-4818.

doi: 10.1007/s11665-021-05919-6

37. Mukherjee T, Elmer JW, Wei HL, *et al.* Control of grain structure phases and defects in additive manufacturing of high-performance metallic components. *Prog Mater Sci*. 2023;138:101153.

doi: 10.1016/j.pmatsci.2023.101153

38. Zheng B, Haley JC, Yang N, *et al.* On the evolution of microstructure and defect control in 316L SS components fabricated via directed energy deposition. *Mater Sci Eng A*. 2019;764:138243.

doi: 10.1016/j.msea.2019.138243

39. Lu QY, Wong CH. Additive manufacturing process monitoring and control by non-destructive testing techniques: Challenges and in-process monitoring. *Virtual Phys Prototyp.* 2018;13:39-48.

doi: 10.1080/17452759.2017.1351201

40. He W, Shi W, Li J, Xie H. *In-situ* monitoring and deformation characterization by optical techniques; part I: Laser-aided direct metal deposition for additive manufacturing. *Opt Laser Eng*. 2019;122:74-88.

doi: 10.1016/j.optlaseng.2019.05.020

41. Zhang X, Shen W, Suresh V, *et al. In situ* monitoring of direct energy deposition via structured light system and its application in remanufacturing industry. *Int J Adv Manuf Technol*. 2021;116:959-974.

doi: 10.1007/s00170-021-07495-4

Appendices

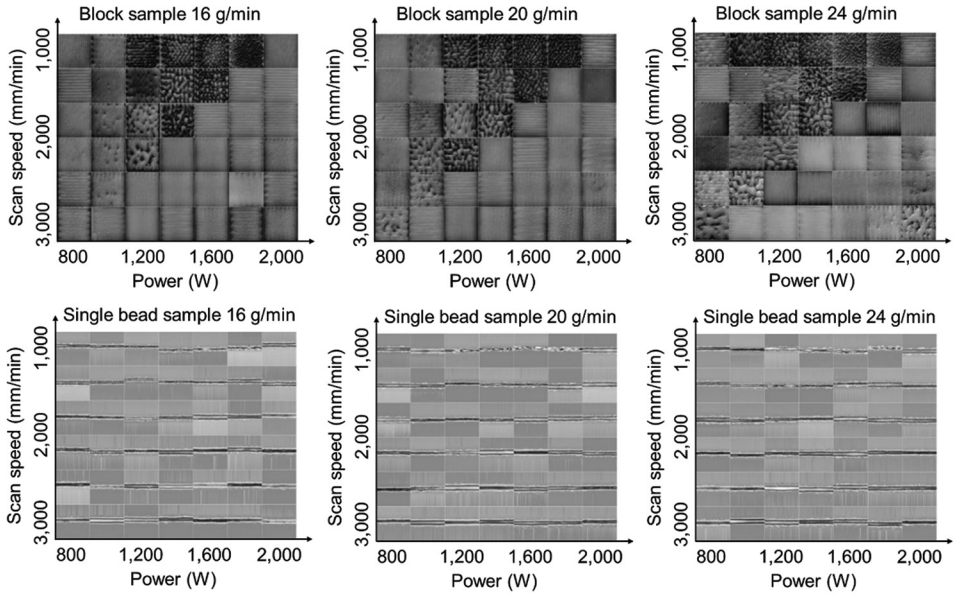

Figure A1. Surface profiles for block samples (top row) and bead samples (bottom row). Each figure represents a unique combination of print parameters, including variations in scanning speed, power, and feed rate.

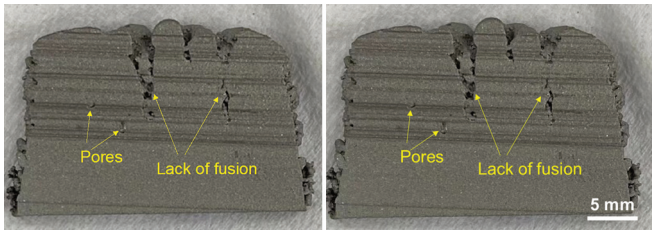

Figure A2. Cross-section of a printed block sample with defects inside the sample, which sacrifices the production of tensile specimens. Scale bar: 5 mm.